Applied Physics A (2026) 132:507
https://doi.org/10.1007/s00339-026-09620-0

Applied Physics A
Materials Science & Processing

Voltage-induced architectural control and interfacial phonon modulation in Cu–Fe functionalized TiO_2 nanotubes

J. O. D Malafatti[1] · E. C. Paris[1] · D. E. Bernal Lozano[2] · J. J. Barba-Ortega[2] · M. Rincón Joya[2]

Received: 5 March 2026 / Accepted: 16 April 2026

Abstract

This study explores the link between voltage-controlled architectural engineering and the resulting lattice dynamics in Cu–Fe functionalized TiO_2 nanotubes. By systematically tuning the anodization potential (30-40 V) and time (40-60 min), we successfully tailored the nanotubular morphology and interfacial structure, as verified by XRD, Raman spectroscopy, and SEM analyses. This work is to elucidate how these structural modifications influence govern the fundamental thermodynamic behavior of the system. Through temperature-dependent heat capacity (C_p) measurements in the 2-300 K range, we reveal a complex vibrational beyond conventional. In the low-temperature regime, deviations from ideal Debye behavior by a Schottky-type contribution indicate a defect rich interfacial environment, where oxygen vacancies and structural disorder introduce discrete energy-level splittings. As temperature increases (50-210 K), a hybrid Debye-Einstein model suggests structural stiffening in the functionalized nanotubes. This effect is reflected in the upward shift of the characteristic phonon temperatures (θ_D and θ_E), indicating increased lattice rigidity and modified sound velocity within the nanotubular framework. Thermodynamic integration up to 298.15 K further demonstrates that the system's free-energy balance is predominantly governed by vibrational entropy rather than internal energy accumulation. These results suggest that the performance of functionalized semiconductors arises not solely from composition, but from nanoscale architectural features that influence phonon-related behavior.

Keywords Anodized · Titanium · Phonon dynamics · Heat capacity · Debye–Einstein model · Cu–Fe functionalization

1 Introduction

Titanium dioxide (TiO_2) has been extensively studied due to its wide range of applications, including photoelectrochemical water splitting, water and air purification, solar energy conversion, biomedical devices, gas sensors, and supercapacitors. These applications arise primarily from the semiconductor properties, chemical stability, and tunable surface characteristics of TiO_2. Various synthesis methods for TiO_2 have been reported in the literature [1–3]. Among them, electrochemical anodization has been widely used because it allows the formation of well-defined nanostructured architectures directly on titanium substrates [2, 3]. Depending on the electrolyte composition, different TiO_2 morphologies can be obtained. In fluoride-free electrolytes, compact oxide films are typically formed, whereas electrolytes containing fluoride ions promote the development of porous structures and highly ordered TiO_2 nanotube arrays. These nanotubular architectures provide large surface area, improved charge transport pathways, and enhanced

J. O. D Malafatti, E. C. Paris, D. E. Bernal Lozano and J. J. Barba-Ortega contributed equally to this work.

✉ M. Rincón Joya
mrinconj@unal.edu.co

J. O. D Malafatti
jmalafatti@hotmail.com

E. C. Paris
elaine.paris@embrapa.br

D. E. Bernal Lozano
debernall@unal.edu.co

J. J. Barba-Ortega
jjbarbao@unal.edu.co

[1] Nanotechnology National Laboratory for Agriculture (LNNA), Embrapa Instrumentação, XV de Novembro st., 1452, 13560-970, São Carlos, SP, Brazil

[2] Departamento de Física, Universidad Nacional de Colombia, Carrera 45 N 26-85, Bogotá 11001, D.C., Colombia

Published online: 15 May 2026

interfacial properties, making them suitable for various applications [2, 4].

Among the different synthesis methods, electrochemical anodization of titanium sheets has been widely used for producing well-defined TiO_2 nanostructures. In this process, the titanium substrate acts as the anode in an electrochemical cell and undergoes oxidation in an electrolyte under an applied potential. The competition between oxide growth and field-assisted dissolution leads to the formation of self-organized oxide structures on the surface. By adjusting parameters such as the applied voltage, electrolyte composition, and anodization time, different morphologies can be obtained, ranging from compact oxide layers to highly ordered TiO_2 nanotube arrays.[5–9]. In this electrochemical process, the titanium substrate acts as the anode in an electrolyte, leading to the formation of an adherent oxide film on the surface. Depending on the anodization conditions, the oxide layer may exhibit porous structures with thicknesses ranging from a few nanometers to several micrometers. Control of the applied voltage governs the rate of oxide growth and the characteristic dimensions of the nanostructures, while longer anodization times generally promote thicker oxide layers. However, excessively high voltages may lead to irregular growth or structural damage, whereas low voltages can result in thinner or incomplete oxide films. These characteristics make anodized TiO_2 suitable for techological application, including aerospace and biomedical fields, where improved corrosion resistance and biocompatibility are desirable [9–16].

The versatility of TiO_2 nanotube architectures has stimulated extensive research in areas ranging from solar energy conversion to biomedical applications, mainly due to their tunable semiconductor properties and high surface area. In addition to morphological control, further modification of TiO_2 nanotubes can be achieved through surface functionalization with transition metals. In particular, the incorporation of copper (Cu) and iron (Fe) introduces interfacial states that can modify the electronic structure, optical band gap, and magnetic response of the material. Beyond these effects, metal–oxide interfaces may also influence the lattice dynamics of the system by altering the phonon spectrum through defect formation and interfacial coupling. Despite the large number of studies focusing on structural and optical properties of anodized TiO_2 nanotubes, the relationship between architectural control, metal functionalization, and the resulting phonon behavior remains less explored [17, 18]. Thermodynamic investigations of TiO_2 nanostructures remain relatively scarce compared to the extensive literature on their optical and catalytic properties. One of the earliest experimental studies was reported by Dames et al.[19], who measured the specific heat of anatase TiO_2 nanotubes in the 1.5–95 K range and reported deviations from bulk behavior due to low-dimensional phonon effects. Subsequent studies have examined the heat capacity of TiO_2 nanostructures such as nanoparticles and nanowires, revealing strong size-dependent contributions associated with surface phonons and lattice disorder [20]. In particular, calorimetric investigations of TiO_2 have shown that the temperature dependence of the heat capacity can be successfully described using combined Debye–Einstein models, enabling the evaluation of thermodynamic functions such as entropy and enthalpy [21] . Despite these advances, most previous work has focused on pristine TiO_2 nanostructures, while the thermodynamic behavior of metal-functionalized TiO_2 nanotube systems remains largely unexplored.

In this context, temperature-dependent heat capacity measurements provide a sensitive thermodynamic probe for investigating lattice dynamics in nanostructured oxides. The analysis of $C_p(T)$ allows access to the phonon density of states and to low-energy excitations associated with defects and interfaces. In the present work, Cu–Fe functionalized TiO_2 nanotube nanocomposites obtained through voltage-controlled anodization are investigated. Structural, morphological, Raman, and thermal analyses are combined to understand how architectural control and interfacial modification influence the vibrational behavior of the system. Heat capacity measurements in the 2–300 K range were analyzed using a Debye–Einstein model to evaluate the role of Cu–Fe functionalization on phonon dynamics. By correlating colorimetric results with structural and spectroscopic characterization, we examine the relationship between voltage-induced architecture, interfacial phonon modulation, and the resulting thermodynamic properties of TiO_2 nanotube systems.

2 Materials and instrumentation

In this study, a commercial titanium film with a thickness of 0.03 mm and a purity of 99.6% (grade 2) was used as the substrate. Prior to the experiments, the titanium film was cleaned to remove surface contaminants. The samples were ultrasonically cleaned in isopropyl alcohol for 15 min and subsequently dried in air at room temperature. The electrolyte solution used for the anodization process consisted of ethylene glycol ($C_2H_6O_2$, Sigma-Aldrich), ammonium fluoride (NH_4F, Panreac), hydrofluoric acid (HF, 40 wt.%, Panreac), and distilled water, following procedures reported in previous studies [22–26].

In the anodization process, titanium foil was used as both the anode. The electrolyte consisted of ethylene glycol (EG), ammonium fluoride (NH_4F), hydrofluoric acid (HF),

Table 1 The samples were annealed at 350°C for 2 h after anodization. Copper and iron were subsequently deposited, followed by calcination at 450°C for 2 h. Sample 1 was anodized at 30 V and sample 2 at 40 V

volts	sample	time (min)	compounds-Ti	compounds-O	compounds-Fe	compounds-Cu
30	1A	40	✓	✓		
30	1B	60	✓	✓		
30	1C	40	✓	✓	✓	✓
30	1D	60	✓	✓	✓	✓
40	2A	40	✓	✓		
40	2B	60	✓	✓		
40	2C	40	✓	✓	✓	✓
40	2D	60	✓	✓	✓	✓

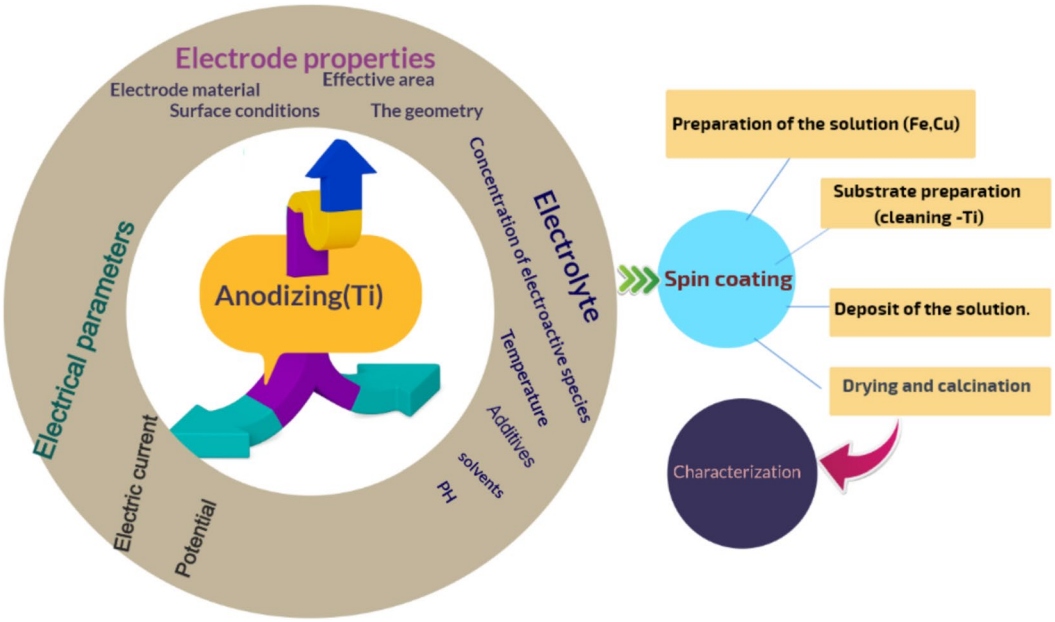

Fig. 1 The schematic illustrates the anodization of the titanium film and the subsequent deposition of copper and iron nanoparticles by the spin-coating method

and distilled water. The anodization experiments were carried out in a two-electrode electrolytic cell with an interelectrode distance of 2 cm. The process was performed under potentiostatic (constant voltage) conditions at room temperature. The electrolyte composition was 65 mL of ethylene glycol, 3 mL of HF, 2 mL of distilled water, and 0.30 g of NH_4F. Anodization was conducted at applied voltages of 30 and 40 V for durations of 40 and 60 min. The experimental parameters and the corresponding sample nomenclature are summarized in Table 1.

Figure 1 shows a schematic representation of the main parameters involved in the anodization process, followed by deposition of copper and iron nanoparticles. Thin films of copper and iron oxides were deposited onto the anodized titanium substrate using the spin-coating. The precursor solution was prepared by dissolving copper and iron salts in a glycerol–water solvent mixture. After this step, the samples were subjected to an annealing treatment to promote the formation of oxide nanoparticles.

The optical characterization of the nanotube samples was carried out using a UV–Vis spectrophotometer (Cary 5000) operating in diffuse reflectance mode. Structural characterization was performed by X-ray diffraction (XRD) using a PANalytical Empyrean diffractometer in Bragg–Brentano geometry at room temperature. The measurements were performed in continuous mode with a step size of 0.02° in the 2θ range from 10° to 90°. The annealing process was carried out in a Vulcan 3-1750 furnace with a heating rate of 20 °C min^{-1} up to 450°C, and maintained for 2 h. Elemental analysis was performed by energy-dispersive X-ray spectroscopy (EDS) using a JEOL JSM-6510 scanning electron microscope. Raman scattering measurements were performed using a Jobin-Yvon T64000 triple monochromator equipped with a CCD detector, using a 532 nm excitation laser. Heat capacity measurements were carried out using a PPMS DynaCool system (Quantum Design) employing the thermal relaxation (two-τ) method in the temperature range from 2 to 210 K.

3 Results

Figure 2 shows the X-ray diffraction (XRD) pattern of the metallic titanium substrate in sheet form prior to any surface modification. All observed reflections can be indexed according to the ICDD/JCPDS card PDF No. 00-044-1294, confirming the presence of metallic titanium without detectable secondary phases. The well-defined diffraction peaks indicate a high degree of crystallinity, which is characteristic of titanium foils produced by industrial rolling processes. The reflections corresponding to the crystallographic planes (100), (002), (101), (102), (110), (103), and (112) match with the angular positions reported for hexagonal metallic titanium [27].

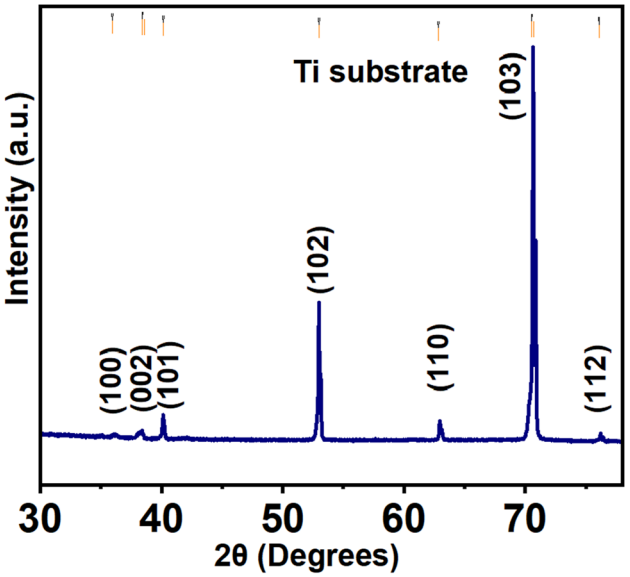

Fig. 2 X-ray diffraction analysis of the titanium foil used as the substrate

Figure 3 presents the X-ray diffraction patterns of samples anodized at 30 V with anodization times of 40 min (1A and 1C) and 60 min (1B and 1D), all calcined at 450 °C. In samples 1C and 1D, Fe and Cu were additionally deposited onto the surface by spin coating after the formation of the TiO_2 nanotubes. The diffraction patterns are mainly composed of the reflections of metallic Ti, indicating that the anodized oxide layer remains relatively thin, which is characteristic of nanotubular architectures [28]. This observation is consistent with anodization followed by thermal treatment leading to surface oxidation without complete. Moreover, increasing the anodization time from 40 to 60 min does not lead to the appearance of additional crystalline phases, suggesting that the main effect of the anodization time is associated with changes in nanotube morphology and oxide layer thickness rather than with long-range crystallographic phase transitions.

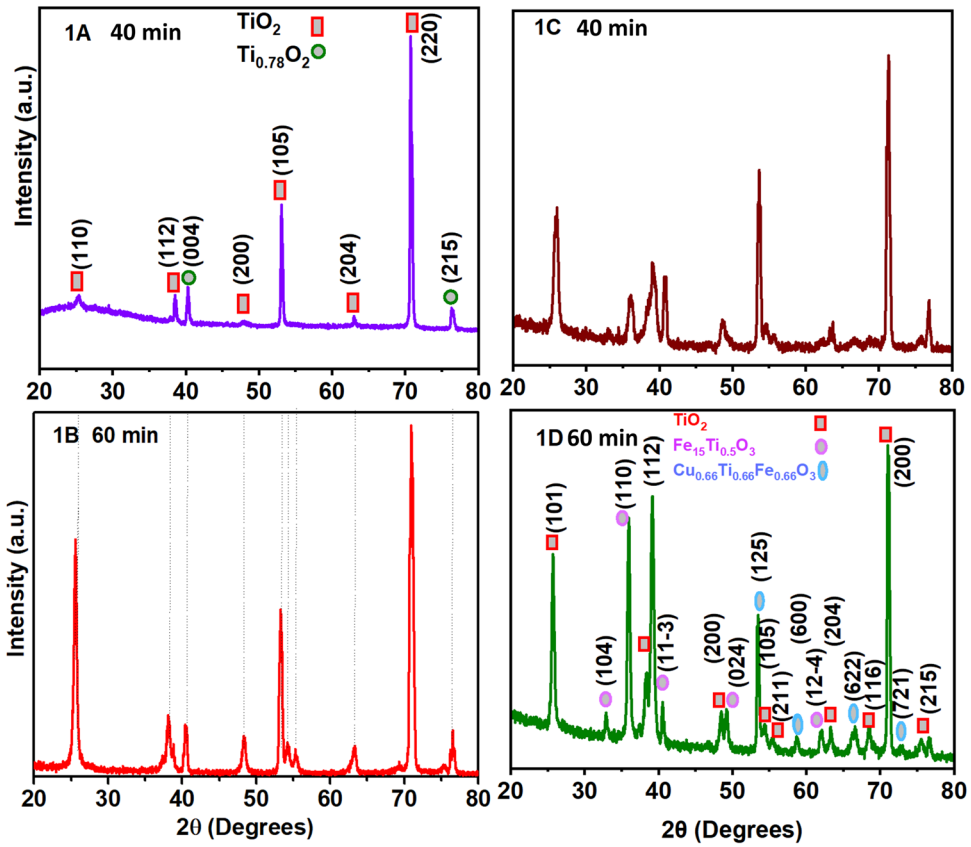

Fig. 3 X-ray diffraction (XRD) patterns of anodized samples: (1A) 30 V for 40 min; (1B) 30 V for 60 min; (1C) 30 V for 40 min followed by Cu and Fe deposition by spin coating; and (1D) 30 V for 60 min followed by Cu and Fe deposition by spin coating. All samples were calcined at 450°C for 2 h after anodization and, when applicable, after metal deposition

In contrast, samples 1C (40 min) and 1D (60 min), which were surface-coated with Fe and Cu by spin coating, exhibit additional diffraction patterns. Besides the reflections attributed with oxide phases involving Fe and Cu species. These features indicate that the metallic species deposited on the nanotube surface undergo oxidation and interact with TiO_2 matrix during possibly leading to the formation of secondary oxide phases [29]. This behavior suggests a thermally induced interfacial interaction between the deposited metals and the TiO_2 nanotube framework, promoting the formation of mixed oxide structures at the surface.

The persistence of intense reflections from metallic Ti indicates that the anodized oxide layer remains relatively thin, which is characteristic of nanotubular architectures. No additional secondary phases were detected. Increasing the anodization time from 40 to 60 minutes does not introduce new crystalline phases, suggesting that its main effect is associated with changes in nanotube morphology and oxide layer thickness rather than to long-range structural phase transformations [28, 29].

As shown in Fig. 3, the X-ray diffraction patterns also reveal weak reflections attributable to anatase TiO_2 (PDF 00-002-0406 / 01-071-1167), located at the characteristic angular positions around ~ 25° (101), ~ 48° (200), ~ 54° (105), ~ 62–63° (204), and ~ 75° (215)/(220), confirming the crystallization of the oxide layer after annealing at 450 °C. In sample 1A, additional contributions consistent with non-stoichiometric titanium oxides (PDF 10-086-1155, $Ti_{0.78}O_2$) are observed, suggesting the presence of a partially reduced Ti/TiO_2 interfacial region enriched in structural defects and oxygen vacancies. In contrast, the spin-coated samples (1C and more prominently 1D) display increasingly additional diffraction patterns due to the appearance of additional reflections associated with Fe and Cu containing oxide phases(PDF 01-089-2812 and 01-078-1627). These results suggest that the Fe–Cu species deposited on the nanotube surface may interact with the TiO_2 surface during annealing likely favored by the high surface area and enhanced reactivity of the nanotubular architecture [30].

In Fig. 4, the X-ray diffraction patterns of the samples anodized at 40 V (2A and 2B) show only minor differences compared with those obtained at lower anodization voltages, suggesting that the overall crystalline phase composition remains essentially unchanged. The diffraction patterns continue to be mainly composed of reflections from the metallic Ti substrate, while the anatase TiO_2 peaks are preserved at their characteristic angular positions. The main effect of increasing the anodization voltage is a moderate increase in the intensity of the anatase reflections, which may indicate improved crystallinity or a slightly higher effective oxide fraction, rather than the formation of additional crystalline

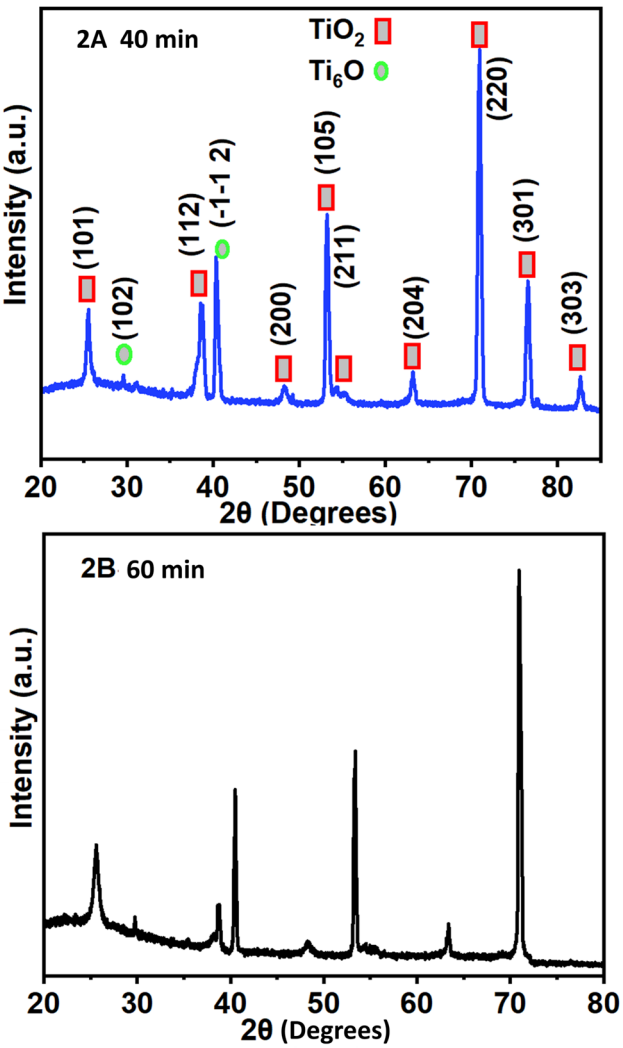

Fig. 4 X-ray diffraction (XRD) patterns of TiO_2 nanotube samples anodized at 40 V: 2A) 40 min and 2B) 60 min anodization time. Both samples were calcined at 450 °C

phases [31–33]. Overall, the XRD analysis indicates that the anodization conditions primarily influence the crystallinity and effective thickness of the TiO_2 nanotube layer without inducing major phase transformations. These structural characteristics are relevant for understanding the subsequent morphological, vibrational, and thermodynamic behavior of the system.

In Figure 5a, the optical absorption edge located at approximately 2.9 eV lies below the nominal band gap of anatase TiO_2 (≈3.1–3.2 eV). This behavior is commonly attributed to sub-gap absorption tails associated with structural and electronic disorder, including defect states such as oxygen vacancies, Ti^{3+} species, and interface states at the nanotube–substrate boundary, rather than to an intrinsic narrowing of the band gap [32, 33]. In contrast, Figure 5b exhibits a sharper and well-defined absorption edge, indicating a reduction in sub-gap states and improved structural

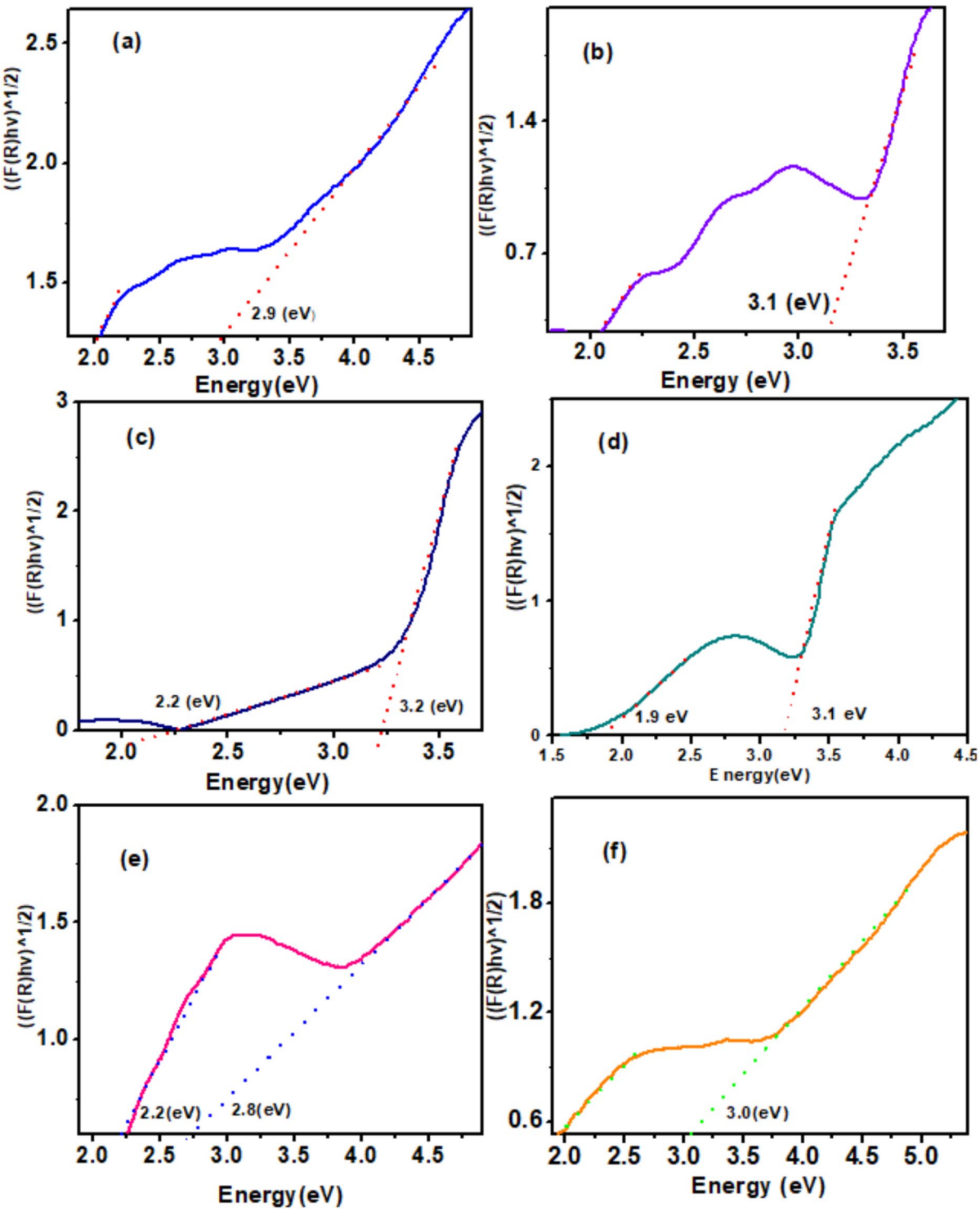

Fig. 5 Tauc plots derived from UV–Vis diffuse reflectance spectroscopy (DRS) using the Kubelka–Munk transformation for optical band-gap determination of TiO_2 nanotube arrays annealed at 450 °C. Indirect allowed electronic transitions were assumed. a) 1A: anodized at 30 V for 40 min; b) 1B: anodized at 30 V for 60 min; c) 1C: anodized at 30 V for 40 min with Cu/Fe deposition onto TiO_2 nanotubes; d) 1D: anodized at 30 V for 60 min with Cu/Fe deposition; e) 2A: anodized at 40 V for 40 min; and f) 2B: anodized at 40 V for 60 min

order associated with the longer anodization time and subsequent annealing, yielding a band-gap value close to 3.1 eV, characteristic of well-crystallized anatase TiO_2 [33].

In Figure 5c (sample 1C), two optical absorption edges can be distinguished: a high-energy transition at ∼3.2 eV corresponding to the fundamental band-gap transition of TiO_2, and a lower-energy edge at ∼2.2 eV associated with visible-light absorption introduced by Cu and Fe related species and/or interfacial states. In Figure 5d (sample 1D), the visible absorption edge shifts further to ∼1.9 eV, suggesting a stronger contribution from CuO/Cu–O–Fe containing oxide species or an increased density of deposition-induced defect states, while the TiO_2-related transition remains essentially unchanged at ∼3.1 eV [32].

In Figure 5e (sample 2A, 40 V, 40 min), the apparent optical gap falls below ∼2.8 eV, which can be attributed to a dominant contribution from defect surface state mediated absorption associated with enhanced optical disorder. In contrast, Figure 5f (sample 2B, 40 V, 60 min) displays a near UV absorption edge at ∼3.0 eV, indicative of a more bulk-like optical response of TiO_2. Overall, the slight downshift of the optical edge observed in the pristine samples is more plausibly related to defect mediated sub band gap absorption tails arising from anodization-induced disorder and residual populations of Ti^{3+} species and oxygen vacancies, rather than to a genuine narrowing of the intrinsic TiO_2 band gap [31, 32]. To correlate the optical response with the structural characteristics of the anodized layers, the morphology and nanotubular architecture of the samples were further examined by SEM.

As observed in the SEM micrographs, electrochemical anodization at 30 V for 40 min leads to the formation of a uniform nanotubular oxide layer, as shown in Fig. 6c. Figure 6a presents the pristine titanium surface prior to anodization, characterized by a relatively smooth morphology. After anodization (Fig. 6b), the surface exhibits the initial formation of the nanotubular oxide layer, although residual electrolyte species are likely present. Following thermal treatment at 450 °C for 2 h (Fig. 6c), a well-defined and homogeneous TiO_2 nanotubular architecture is obtained. This thermal step is associated with the removal of residual electrolyte and improved the structural integrity of the oxide layer, resulting in a more stable and uniform nanotubular coating [34].

All samples were prepared during the anodization process using the same electrolyte composition, as described in the previous section. The anodization time was set at 40 and 60 min, with applied potentials of 30 and 40 V. After anodization, the samples were thermally treated at 350 °C for 2 h to reduce residual electrolyte species. The anodized Ti films were then cleaned and used as substrates for the deposition of Cu and Fe by spin-coating. Finally, all samples were calcined at 450 °C to stabilize the oxide layer and the deposited species.

In the anodization process, the evolution of the current density as a function of time is typically monitored, as reported in the literature [22, 23]. When a constant voltage is appled, the formation of a porous oxide layer leads to a characteristic current density time curve. The kinetics of this process can generally be divided into three distinct stages. The first stage is characterized by a rapid decrease in current density, corresponding to the initial formation of a compact oxide barrier layer on the Ti surface. This layer exhibits high electrical resistance and forms through the electrochemical interaction between Ti^{4+} ions and O^{2-} species derived from the electrolyte [35]. The overall anodic reaction can be expressed follows:

$$Ti + 2H_2O \rightarrow TiO_2 + 4e^- + 4H^+ \quad (1)$$

The current density increases until reaching a maximum value, corresponding to the onset of pore formation. This results areassociated with the field-assisted chemical dissolution of the initially formed oxide layer, in the presence of fluoride ions present in the electrolyte. Under the influence of the electric field established between the electrodes, localized dissolution occurs at the oxide/electrolyte interface, initiating the development of nanopores. The dissolution process can be described by the following reaction [35]:

$$TiO_2 + 6F^- + 4H^+ \rightarrow TiF_6^{2-} + 2H_2O \quad (2)$$

At longer times, the current density reaches a nearly steady value, indicating a dynamic equilibrium between oxide

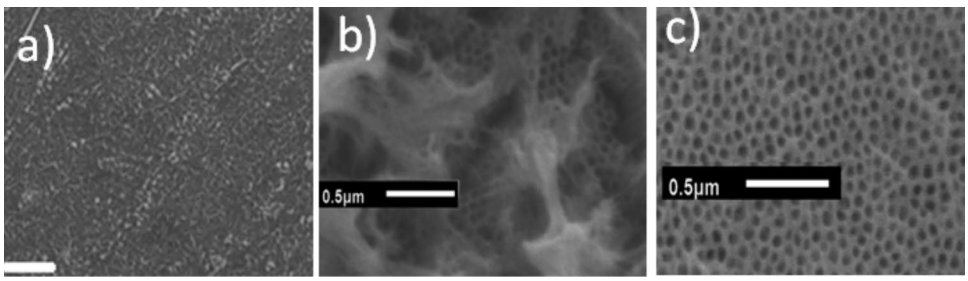

Fig. 6 SEM micrographs of the titanium substrate: **a**) pristine Ti; **b**) anodized Ti; and **c**) anodized Ti after thermal treatment at 350 °C for 2 h

formation and field-assisted dissolution, which leads to the growth of TiO_2 nanotubes and marks the completion of the anodization stage. Detailed analyses of the current density evolution as a function of time, voltage, and electrolyte composition can be found in previous studies [22, 23, 25, 36]. After completion of the anodization process and subsequent drying of the samples, copper and iron nanoparticles were deposited onto the anodized TiO_2 nanotube layers.

Figures 7a and 7b show FESEM images of the TiO_2 nanotubes obtained at an anodization potential of 30 V with an anodization time of 40 min (sample 1A). Figure 7a presents the surface morphology after thermal treatment, revealing open and uniformly distributed nanotubes across the surface. In Figure 7b, a fracture produced using a clamp allows observation of the lateral morphology and thickness of the nanotubular layer. Figures 7c and 7d correspond to the sample anodized for 60 min at 30 V (sample 1B). In Figure 7c, traces left mechanical removal of nanotubes with tweezers are observed, confirming the uniform distribution of the nanotubular array. Figure 7d shows a fractured region where the nanotubes appear longer than in the 40 min samples, indicating a progressive increase in nanotube length with increasing anodization time.

In Figures 8a, 8c, and 8e, the morphology of sample 1C anodized at 30 V for 40 min and subsequently modified by Cu and Fe deposition via spin coating is shown. In Figure 8a, the inset image shows a uniform nanotubular substrate with open and well defined nanotube mouths. A layered surface structure can also be distinguished, consisting of the underlying nanotube array followed by elongated nanoparticles aggregates and, above them, particles exhibiting a lamellar morphology. In Figure 8c, clusters of rice like nanoparticles are observed beneath a hierarchical surface structure distributed across the surface. Finally, the cross-sectional fracture in Fig. 8e shows the presence of a Cu–Fe particle layer formed on top of the TiO_2 nanotubes.

Figures 8b, 8d, and 8f correspond to sample 1D anodized at 30 V for 60 min. Figure 8b displays a homogeneous dispersion of elongated nanoparticles on the nanotubular surface. In contrast to Fig. 8c, the hierarchical morphology is not observed in Fig. 8d; instead, only a single type of nanoparticle morphology is present which indicates. The fractured region shown in Fig. 8f confirms the formation of a Cu–Fe particle layer on the nanotubes, although this layer appears slightly thinner than that observed for the sample anodized for 40 min [37].

Figure 9a illustrates the sample anodized at 40 V for 40 min. The surface exhibits open TiO_2 nanotubes, although slight morphological irregularities are observed compared with those formed at 30 V. Figure 9b shows the fractured sample anodized at 40 V for 60 min, where the nanotubular architecture remains visible along the cross-section. Figures 9c and 9d correspond to the sample anodized at 40 V for 40 min after deposition of Cu and Fe particles. In Figure 9c, aggregates composed of elongated nanoparticles are observed on the nanotubular surface. Figure 9d provides a higher magnified view of these nanoparticles, which appear uniformly distributed with a relatively narrow size distribution [37].

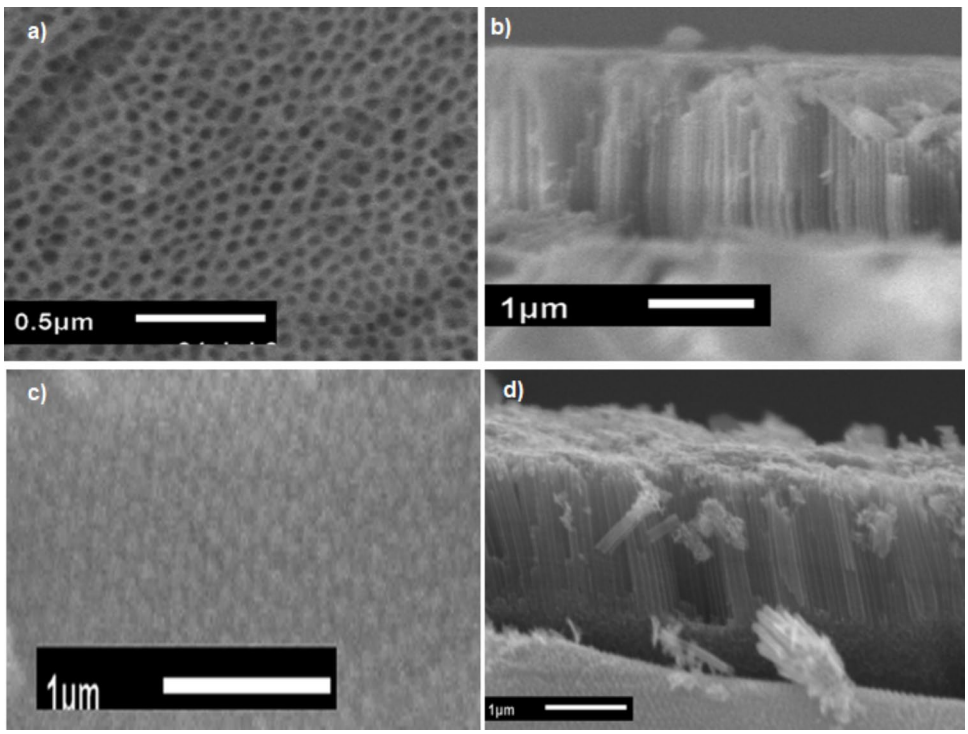

Fig. 7 FESEM images of TiO_2 nanotubes obtained by anodization at 30 V (method 1). **a**) Surface morphology of sample 1A after 40 min of anodization. **b**) Cross-sectional fracture of sample 1A (40 min). **c**) Traces of nanotubes from sample 1B after mechanical removal using tweezers. **d**) Cross-sectional fracture of sample 1B after 60 min of anodization

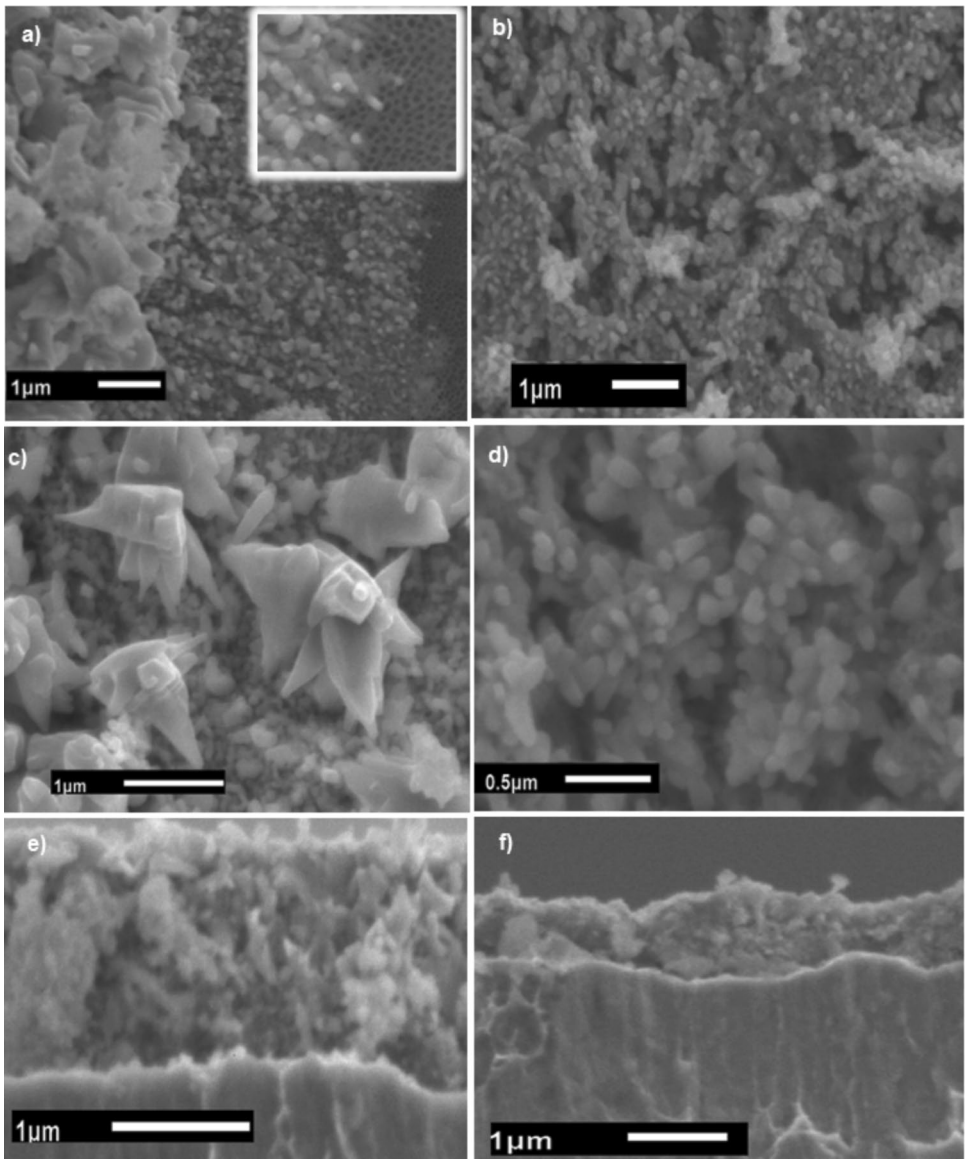

Fig. 8 FESEM images of TiO_2 nanotubes obtained by anodization at 30 V (method 1) after Cu and Fe deposition. Sample 1C: a) surface morphology showing the nanotube openings with Cu and Fe particles; c) general surface exhibiting a flower-like morphology; e) cross-sectional fracture of the sample. Sample 1D: b) surface morphology of the sample; d) magnified view of the nanotubular surface; f) cross-sectional fracture of the sample

In addition, Figures 9e and 9f correspond to the sample anodized at 40 V for 60 min with Cu and Fe deposition (sample 2D). In this case, the deposited particles form a compact layered morphology that differs from the particle aggregates observed in Fig. 8. The fractured region shown in Fig. 9f shows that this morphology develops mainly on top of the nanotube layer, suggesting a coalescence of Fe/Cu nanoparticles rather than a destruction of the underlying nanotubular structure. To relate the surface morphology to the chemical composition of the deposited layer, elemental mapping was carried out by energy-dispersive X-ray spectroscopy (EDS).

Figure 10 shows the EDS elemental mapping of samples 1A, 2A, 1B, and 2B. The maps consistent with a homogeneous spatial distribution of Ti and O across the analyzed regions, confirming the formation of a TiO_2 oxide layer over the titanium substrate. In addition, the presence of fluorine is detected uniformly on the surface. This signal is associated with residual fluorinated species originating from the fluoride-containing electrolyte (NH_4F/HF) used during anodization, which participate in the dissolution–growth equilibrium through the formation of soluble $[TiF_6]^{2-}$ complexes [38]. The homogeneous distribution of F is consistent with the presence of Ti–F surface terminations and the high surface area characteristic of the nanotubular architecture.

The nitrogen signal observed in the maps is attributed to residual nitrogen-containing species from the electrolyte (NH_4^+), which may remain weakly adsorbed on the nanotube walls or trapped within the nanotubular channels, particularly in samples with longer anodization times. Although present in low concentration, both F and N species can influence the surface electronic structure by modifying surface

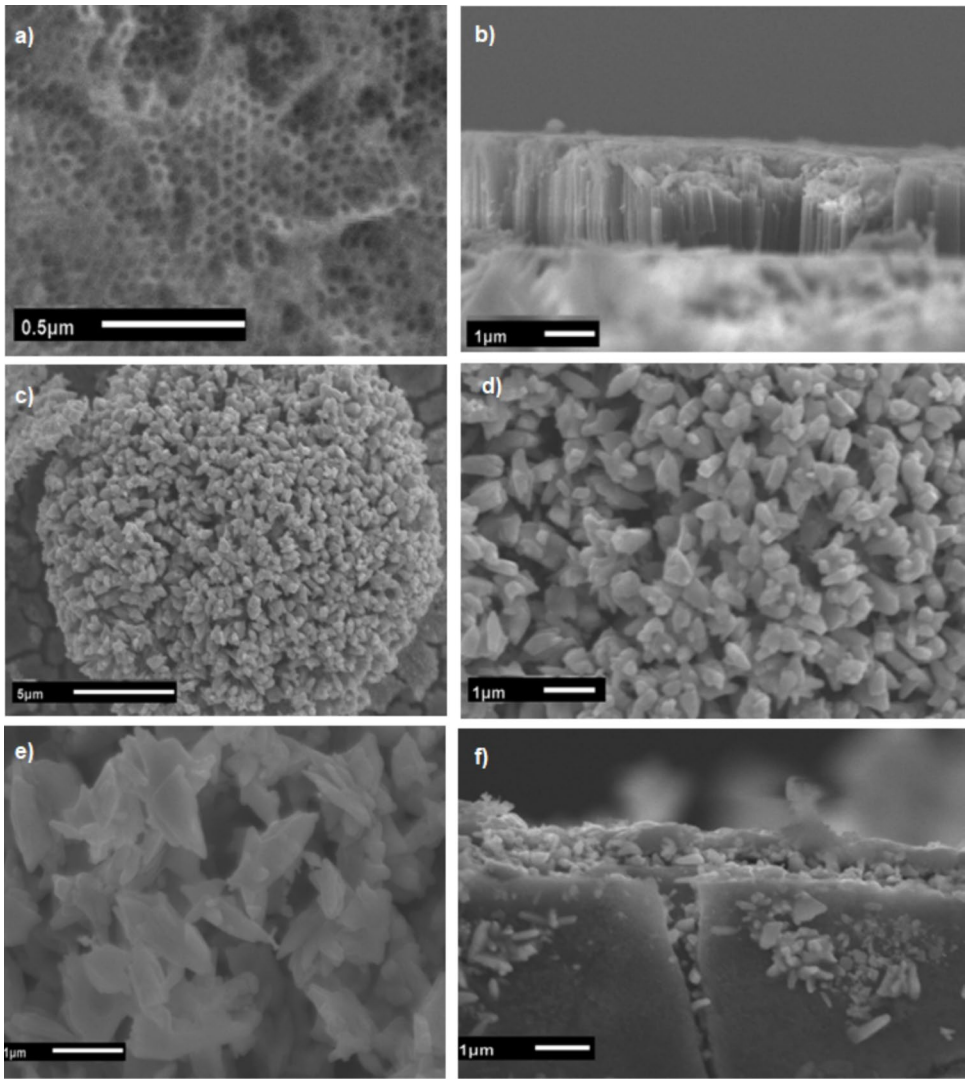

Fig. 9 FESEM images of TiO_2 nanotubes obtained by anodization at 40 V (method 2). a) Sample 2A; b) sample 2B; (c,d) sample 2C; and (e,f) sample 2D

states and band bending, potentially affecting charge transport and trapping processes without altering the crystalline phase of TiO_2 identified by XRD.

The differences between samples 1A/1B (30 V) and 2A/2B (40 V) are mainly related to variations in the anodization voltage and time, which control the electric-field-driven balance between oxide growth, ionic migration, and fluoride-assisted dissolution at the TiO_2/electrolyte interface. As a result, higher voltages and longer anodization times favor deeper electrolyte interaction with the nanotube channels and slightly increased incorporation of fluorinated and nitrogen-containing species within the nanotubular structure.

As shown in Fig. 11, the SEM–EDS analysis of samples 1C, 2C, 1D, and 2D indicates the successful incorporation of Cu- and Fe-based oxide species onto the anodized TiO_2 nanotubular framework. The strong and continuous Ti and O signals indicate that TiO_2 remains the dominant structural matrix after spin-coating deposition and subsequent calcination at 450 °C. In addition, the elemental maps reveal a homogeneous spatial distribution of Cu and Fe across the analyzed regions, suggesting an intimate interfacial interaction between the deposited metal oxides and the TiO_2 nanotube surface. The co-distribution of Cu and Fe signals is consistent with the formation of a mixed Cu–Fe oxide layer dispersed over the TiO_2 nanotubular surface [37]. Raman spectroscopy was employed to further probe the vibrational modes and structural order of the TiO_2 nanotube arrays, complementing the structural and compositional information obtained from XRD, SEM, and EDS analyses.

Figure 12 presents the Raman spectra of the TiO_2 nanotube samples obtained under different anodization conditions and surface modifications. The spectrum of sample 1B (30 V, 60 min) shows the characteristic Raman modes of anatase TiO_2, located at approximately E_g 145 cm^{-1} (most intense), E_g 200 cm^{-1}, B_{1g} 399 cm^{-1}, B_{1g} 514 cm^{-1}, A_{1g} 519 cm^{-1}, and E_g 640 cm^{-1}. These vibrational features are consistent with the presence of the anatase phase, consistent with the XRD results for samples calcined at 450 °C [39].

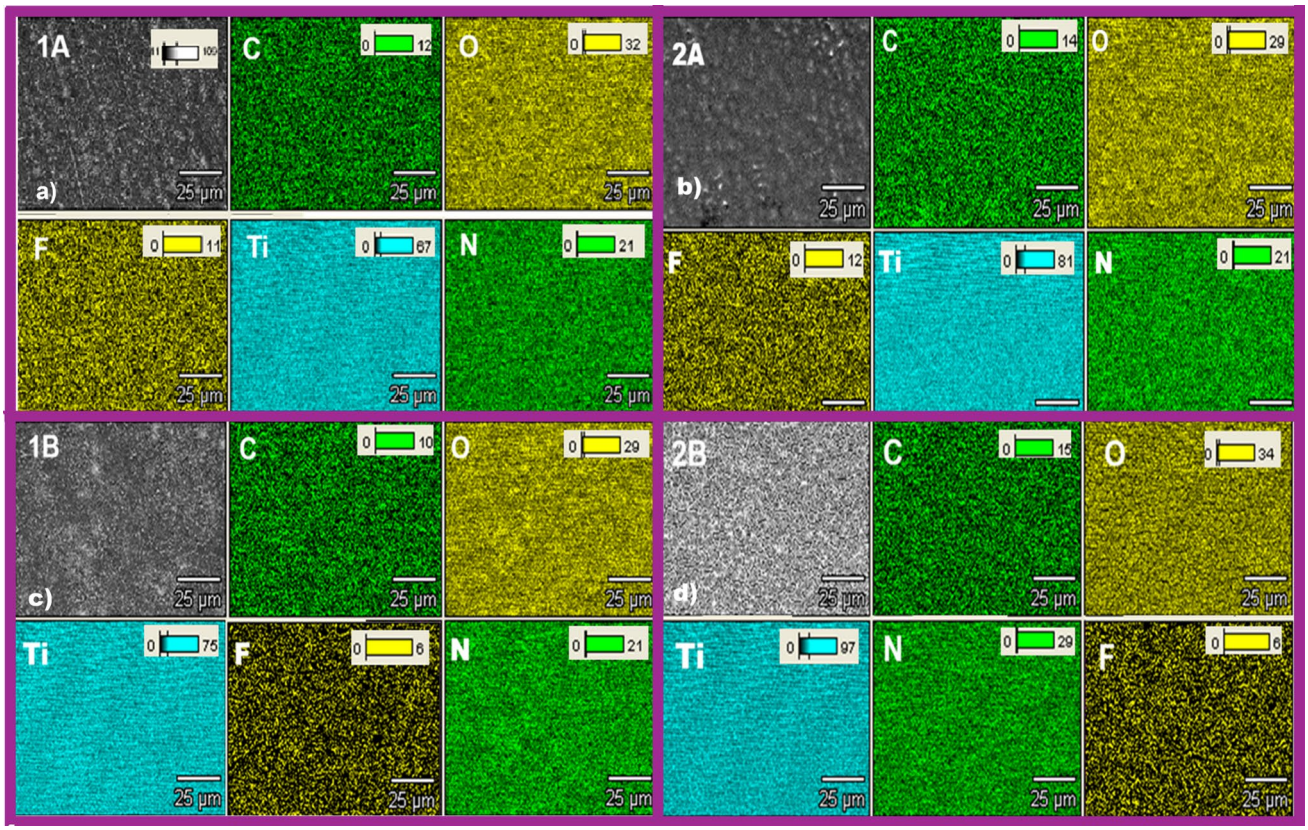

Fig. 10 EDS elemental maps of samples 1A a), 2A b), 1B c), and 2B d), showing the spatial distribution of C, O, Ti, F, and N across the sample surface. The maps reveal a homogeneous distribution of these elements over the analyzed areas. Scale bar: 25 μm

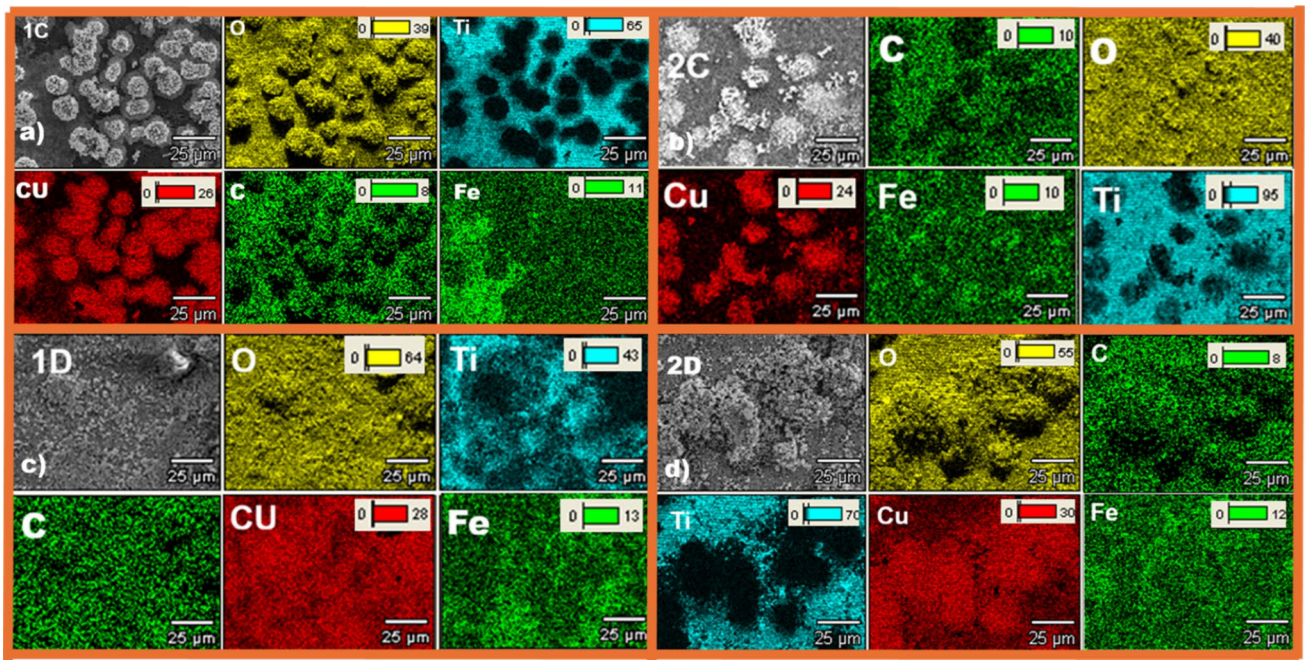

Fig. 11 EDS elemental maps of samples 1C a), 2C b), 1D c), and 2D d), showing the spatial distribution of O, Ti, Cu, Fe, and C. The maps reveal a uniform co-distribution of Ti, Cu, and Fe within an oxygen-rich oxide matrix and a progressively more compact elemental distribution across the analyzed areas. Scale bar: 25 μm

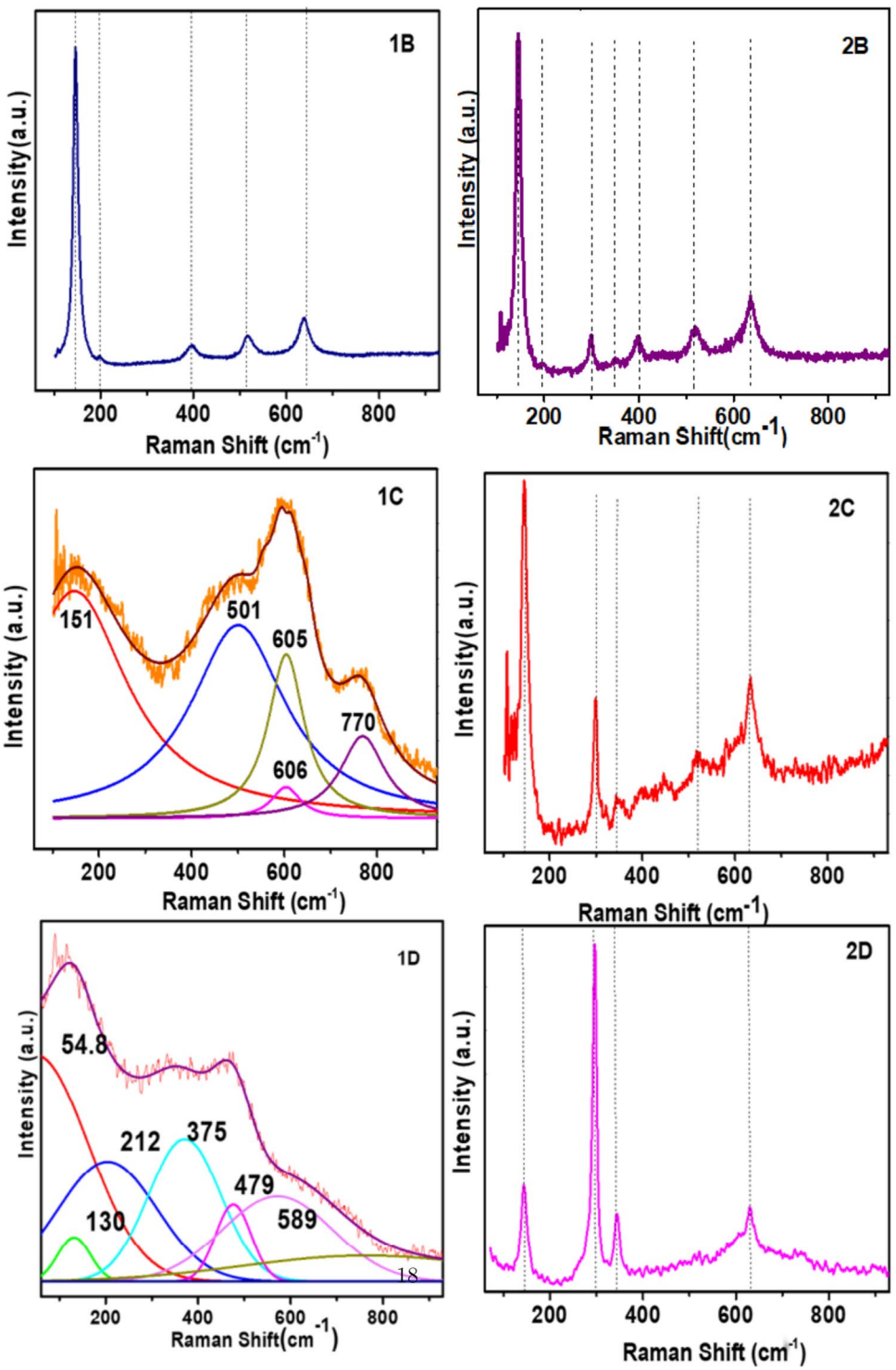

Fig. 12 Raman spectra of TiO_2 nanotube samples obtained under different anodization conditions and surface modifications. **a**) Sample 1B, **b**) sample 2B, **c**) sample 1C with peak deconvolution, **d**) sample 2C, **e**) sample 1D with peak deconvolution, and **f**) sample 2D. The dashed lines indicate the characteristic Raman modes of anatase TiO_2

As observed in Figs. 12 (1B, 2B, 2C, and 2D), the main Raman vibration modes correspond to anatase TiO_2, particularly the intense E_g mode at $\sim 145\,\mathrm{cm}^{-1}$. Minor contributions potentially associated with rutile TiO_2 may appear around ~ 447 and $\sim 612\,\mathrm{cm}^{-1}$, although these signals remain weak. For sample 2B (40 V, 60 min), the anatase fingerprint is preserved. The increase in anodization voltage tends to modifies the nanotube geometry (diameter and wall thickness), increasing the effective scattering volume within the Raman excitation region. In addition, higher anodization voltages may introduce residual strain and point defects, such as oxygen vacancies and Ti^{3+} species, which can manifest as variations in relative peak intensities and moderate band broadening. The slightly elevated background observed in

this spectrum may also be associated with defect-related structural disorder. The appearance of vibrational features in Sample 2B at ~447 cm^{-1} and within the 200-400 cm^{-1} region corresponds to the E_g mode of rutile TiO_2 and the activation of lattice signatures from sub-stoichiometric Ti_6O phases, respectively, indicating a voltage-induced transition toward a more complex, defect-rich interfacial environment [39]. These modes provide spectroscopic evidence of the localized structural disorder and oxygen-deficient growth kinetics that underpin the enhanced lattice rigidity observed at higher anodization potentials [40].

In samples 1C and 1D, following the deposition of Fe and Cu onto the nanotubular TiO_2 surface and subsequent calcination, the Raman spectra exhibit significant band broadening. This effect can be attributed to interfacial modifications at the Fe–Cu/TiO_2 interface, including lattice strain, increased defect density, and local structural disorder. As a result, the weaker anatase modes become partially masked, while additional vibrational contributions appear that may be associated with copper and iron oxides formed during calcination.

Reported Raman bands of CuO are typically located near ~ 298, ~ 346, and $\sim 630\,cm^{-1}$, while α-Fe_2O_3 (hematite) exhibits characteristic modes around ~ 225, ~ 247, ~ 293 , ~ 412, ~ 499, and $\sim 613\,cm^{-1}$. Because several of these modes lie close to TiO_2 vibrational features, spectral overlap occurs, making it difficult to unambiguously identify the dominant oxide phase solely from Raman analysis. The pronounced linewidth broadening further suggests an increased degree of structural disorder associatde with the Fe–Cu surface modification [40].

For sample 2D (40 V, 60 min anodization followed by Fe–Cu deposition and calcination at 450 °C), the Raman spectrum shows significant changes. The dominant anatase E_g mode at $\sim 145\,cm^{-1}$ is strongly attenuated, while the most intense band appears near $\sim 300\,cm^{-1}$. This behavior suggest that the raman response is mainly governed by the Fe–Cu oxide overlayer rather than the underlying TiO_2 nanotubular matrix. The band position is consistent with reported modes of α-Fe_2O_3 ($\sim 293\,cm^{-1}$) and CuO ($\sim 298\,cm^{-1}$), suggesting the formation of iron and copper oxide phases on the surface after calcination [40]. The attenuation of anatase modes and the enhanced band broadening further indicate strong interfacial coupling and increased structural disorder at the Fe–Cu/TiO_2 heterojunction. These results suggest that, for sem, longer anodization times, the surface oxide layer becomes dominant within the Raman probing depth [41]. The contrast in the Raman baseline between the 30 V (1C/1D) and 40 V (2C/2D) series arises from localized structural disorder and a higher density of electronic defect states such as oxygen vacancies and Ti^{3+} rather than macroscopic morphology. The presence of oxygen vacancies and Ti^{3+} defect states in TiO_2 is well known to introduce electronic states within the band gap and to significantly modify the optical and vibrational response of the material, including changes in Raman spectra and optical absorption behavior. Consistently, while these defects are associated with an elevated background in the 30 V samples, the signal in the 40 V series is mainly governed by the more compact Fe-Cu oxide overlayer, which effectively shields the disordered TiO_2 interface [42].

3.1 Heat capacity analysis

Figure 13 presents the temperature dependence of the specific heat for the pristine anodized TiO_2 nanotubes 2B), establishing the thermodynamic reference behavior of the system. The corresponding analysis for the Cu Fe functionalized sample 2D) is shown in Fig. 14, where the upper panel reveals a clear deviation from ideal Debye behavior in the low-temperature region, while the lower panel displays the intermediate temperature regime highlights the Debye–Einstein model. This comparative representation underscores the modification of lattice dynamics associated with surface functionalization [21, 43].

To analyze the experimental heat capacity data, the temperature range was divided into distinct intervals in order to apply the appropriate lattice-dynamical models. In crystalline solids, low energy acoustic phonons are described within the Debye formalism, which accounts for long wavelength collective vibrations, whereas higher energy optical modes are better described by the Einstein model.

Given that TiO_2 is a multi-atomic crystal with several atoms per unit cell, its vibrational spectrum is not fully described by a purely Debye-type approximation. Therefore, a combined Debye–Einstein approach was adopted. The low-temperature region was analyzed within the Debye framework, while intermediate temperatures (50–210 K)

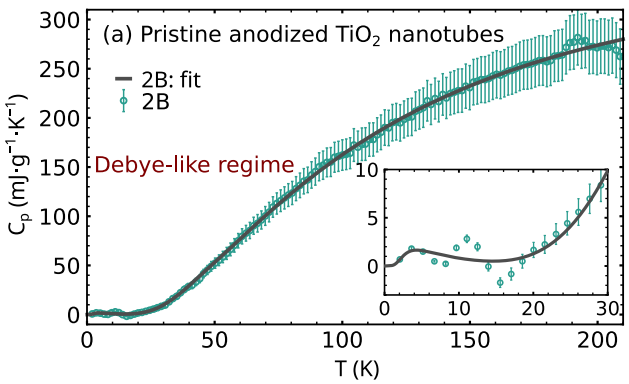

Fig. 13 Temperature dependence of the specific heat of pristine anodized TiO_2 nanotubes 2B). Solid lines correspond to the fitted model described in the text. The inset shows the low-temperature region, highlighting the deviation from ideal Debye behavior

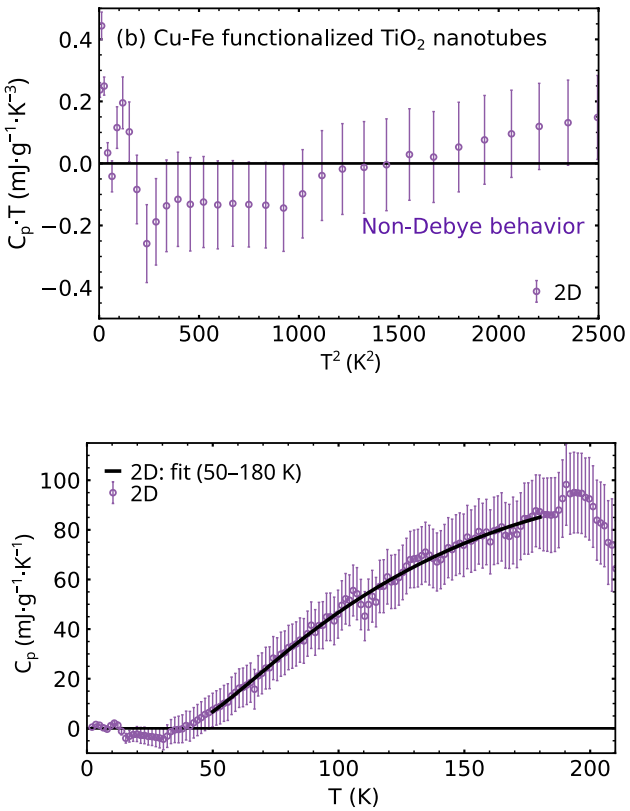

Fig. 14 Specific heat analysis of the Cu–Fe functionalized TiO_2 nanotubes (2D). Top panel: low-temperature region displayed as C_p/T versus T^2, highlighting non-Debye behavior. Bottom panel: intermediate-temperature region fitted using the Debye–Einstein model. Solid lines correspond to the model fits described in the text

were fitted with Einstein contributions associated with localized optical modes, particularly those related to Ti–O bond vibrations. The experimental heat capacity was described by the following expression [43]:

$$C_P(2-40K) = \gamma T + B_3T^3 + B_5T^5 + B_7T^7 + B_9T^9 + n_{Sch}R\left(\frac{\theta_{Sch}}{T}\right)^2 \frac{e^{\theta_{Sch}/T}}{\left(1+e^{\theta_{Sch}/T}\right)^2}$$

$$C_P(40-50K) = A_0 + A_1 \cdot T + A_2 \cdot T^2 + A_3 \cdot T^3$$

$$C_p(50-210K) = n_D\, D(T,\theta_D) + n_E\, E(T,\theta_E),$$

For sample 2D, the following equation was employed:

$$C_p^{\dagger}(50-180K) = n_D\, D(T,\theta_D) + n_E\, E(T,\theta_E), + AT$$

$$D(T,\theta_D) = 9R\left(\frac{T}{\theta_D}\right)^3 \int_0^{\theta_D/T} \frac{u^4 e^u}{(e^u-1)^2}\, du,$$

$$E(T,\theta_E) = 3R\left(\frac{\theta_E}{T}\right)^2 \frac{e^{\theta_E/T}}{\left(e^{\theta_E/T}-1\right)^2}.$$

At low temperatures (2-40 K), the heat capacity was analyzed including possible additional low-energy contributions. In insulating crystalline systems, the dominant term is expected to follow a T^3 dependence arising from acoustic phonons. A negligible linear coefficient γ confirms the absence of an electronic contribution. The inclusion of a Schottky type term allows for of defect-related or interfacial excitations, which may become relevant in nanostructured systems. The linear coefficient (γ) is not attributed to conduction electrons in this system [44], instead, such a linear in temperature contribution is more plausibly associated with lattice defects, particularly vacancy-related disorder that introduces low-energy excitations. The Schottky term (nsR) may arise from defect related surface states of hydroxyl $(-OH)$ groups bound to defect sites, which generate discrete energy-level splitting contributions to the heat capacity. 40–50 K interval was modeled using a third-order polynomial to ensure a smooth crossover between the low- and high-temperature regimes, preserving continuity for thermodynamic integration.

In the 50-210 K range, the experimental $C_{p,m}(T)$ data were described using a Debye–Einstein model,

$$C_p(T) = n_D D(T,\theta_D) + n_E E(T,\theta_E), \tag{3}$$

where the Debye function $D(T,\theta_D)$ represents collective acoustic phonons and the Einstein function $E(T,\theta_E)$ accounts for optical vibrational modes associated with localized Ti-O bonding dynamics. The weighting factors n_D and n_E quantify the relative phonon contributions, while the characteristic temperatures θ_D and θ_E define the corresponding vibrational energy scales. In particular, θ_D provides insight into the effective elastic response of the nanotubular framework [43].

In Table 2, sample 2B exhibits a Schottky type contribution with $\theta_{\mathrm{Sch}} = 10.12$ K. The linear coefficient $\gamma = 3.923 \times 10^{-5}$ is small but finite. For an ideal intrinsic semiconductor, this term should be essentially zero. Its non-zero value suggests a finite density of low-energy electronic states, attributed to structural defects, oxygen vacancies, and surface states associated with the nanotubular morphology of anodized TiO_2.

The Schottky contribution suggests the presence of centers with small energy splitting, consistent with discrete levels induced by point defects and surface-trapped states. These findings are consistent with the defect-rich nature of electrochemically anodized TiO_2. The relatively high RMSE value (222%) suggests that the adopted model does not fully capture the system's complexity, most likely due to the superposition of multiple thermal and electronic processes in the low-temperature regime.

Table 2 Fitted coefficients of the $C_p(T)$ models and derived thermodynamic functions for anodized TiO_2 nanotube samples. Sample 2B corresponds to pristine anodized TiO_2, whereas sample 2D represents the Fe/Cu surface-modified system

Parameter	2B	2D
Low-temperature region (2–40 K), Schottky + power series		
γ (J g^{-1}·K^{-2})	3.923 10^{-5}	–
B_3 (J g^{-1}·K^{-4})	-3.953 10^{-7}	–
B_5 (J g^{-1}·K^{-6})	1.348 10^{-9}	–
B_7 (J g^{-1}·K^{-8})	-7.425 10^{-13}	–
B_9 (J g^{-1}·K^{-10})	1.403 10^{-16}	–
n_{Sch} (g)	4.136 10^{-4}	–
θ_{Sch} (K)	10.12	–
RMSE%	222.5	–
Range (K)	2-40	–
Intermediate region (40–50 K), Polynomial fit		
A_0 (J g^{-1}·K^{-1})	-0.132	–
A_1 (J g^{-1}·K^{-2})	6.861 10^{-3}	–
A_2 (J g^{-1}·K^{-3})	-1.003 10^{-4}	–
A_3 (J g^{-1}·K^{-4})	7.379 10^{-7}	–
RMSE%	5.61	–
Range (K)	40-50	–
High-temperature region (50–210 K), Debye–Einstein model		
n_D (g)	1.016 10^{-2}	5.402 10^{-3}
θ_D (K)	336.9	393.1
n_E (g)	4.194 10^{-3}	3.082 10^{-3}
θ_E (K)	589.6	717.9
A_1 (J g^{-1}·K^{-2})	–	2.545 10^{-4}
RMSE%	1.63	5.16
Range (K)	50-210	50-180
Thermodynamic functions at 298.15 Kel		
$H^{298.15}$ (J g^{-1}·)	58.14	–
$S^{298.15}$ (mJ g^{-1}·K^{-1})	362.7	–

In sample 2B, the 40-50 K interval defines a thermal crossover regime where residual defect related excitations coexist with the progressive activation of lattice phonons. The nonlinear curvature of $C_p(T)$, evidenced by the alternating polynomial coefficients, indicates a smooth transition from localized low-energy states to collective vibrational dominance. The low RMSE (5.61%) supports the robustness of the fit and excludes critical anomalies or phase transitions in this temperature range.

In the 50-210 K regime, the Debye Einstein parameters suggest a structural stiffening associated with the Fe/Cu modification. The increase in θ_D (336.9→393.1 K) indicates an enhancement of the effective lattice rigidity and average sound velocity, while the reduction in the acoustic weight n_D (1.016×10^{-2} →5.402×10^{-3}) indicates a relative suppression of low energy phonon contributions. Consistently, the rise in θ_E (589.6→717.9 K) reflects a shift of optical modes toward higher energies, attributable to strengthened Fe-O and Cu-O bonds, accompanied by a decrease in n_E (4.194×10^{-3} →3.082×10^{-3}), suggesting a redistribution of the phonon density of states. The emergence of the additional A_1 term in 2D indicates a residual electronic or defect-related contribution associated with functionalization. The low RMSE values (1.63% and 5.16%) support the robustness of the model and indicate a clear modification of the vibrational spectrum following surface coating.

For sample 2B at 298.15 K, the evaluation of its energetic and entropic state at ambient conditions was carried out by determining the corresponding thermodynamic functions, which were obtained from the integrated heat capacity:

$$H^{298.15} = \int_0^{298.15} C_p(T)\, dT, \tag{4}$$

$$S^{298.15} = \int_0^{298.15} \frac{C_p(T)}{T}\, dT. \tag{5}$$

For sample 2B, the resulting values are

$$H^{298.15} = 58.14\ \mathrm{J\,g^{-1}}, \qquad S^{298.15} = 0.3627\ \mathrm{J\,g^{-1}\,K^{-1}}. \tag{6}$$

The corresponding thermal Gibbs function,

$$G^{298.15} = H^{298.15} - TS^{298.15}, \tag{7}$$

yields

$$TS^{298.15} = 298.15 \times 0.3627 = 108.14\ \mathrm{J\,g^{-1}}, \tag{8}$$

$$G^{298.15} \approx -50.00\ \mathrm{J\,g^{-1}}. \tag{9}$$

The ratio between entropic and enthalpic contributions,

$$\frac{TS^{298.15}}{H^{298.15}} \approx 1.86, \tag{10}$$

demonstrates that at 298 K the thermal state is predominantly governed by vibrational entropy rather than internal energy accumulation. In other words, the multiplicity of thermally accessible phonon microstates dominates the free-energy balance.

To assess the proximity to the classical Dulong-Petit limit [45, 46]:, the theoretical high-temperature heat capacity for TiO_2 is

$$C_{V,\mathrm{DP}} = 3nR = 9R = 74.83\ \mathrm{J\,mol^{-1}\,K^{-1}}, \tag{11}$$

which corresponds, in mass units, to

$$C_{V,\mathrm{DP}}^{(\mathrm{mass})} = 0.9367\ \mathrm{J\,g^{-1}\,K^{-1}}. \tag{12}$$

Given the extracted characteristic temperatures $\theta_D = 336.9$ K and $\theta_E = 589.6$ K, the ratios

$$\frac{T}{\theta_D} \approx 0.89, \qquad \frac{T}{\theta_E} \approx 0.51, \tag{13}$$

indicate that while the acoustic phonon branch approaches the classical regime at 298 K, a substantial fraction of high-energy optical modes remains partially unpopulated. Therefore, the system has not fully reached the Dulong–Petit limit at ambient temperature and resides in a mixed quantum–classical vibrational regime. This interpretation is consistent with the significant entropic contribution to the Gibbs thermal function and the relatively high Einstein characteristic temperature.

The combined spectroscopic and calorimetric analyses indicate that lattice dynamics in Fe/Cu-modified TiO_2 nanotube systems are influenced by nanoscale morphology and interfacial architecture. The pristine nanotubular framework can be considered as a thermodynamic reference state in which the free energy balance at ambient temperature is dominated by vibrational entropy. In contrast, the Fe/Cu-modified architecture, characterized by layered oxide domains anchored to the nanotube walls, exhibits increased Debye and Einstein characteristic temperatures together with Raman observed phonon sharpening, indicating enhanced lattice rigidity associated with metal oxide interfacial coupling. Across the different morphologies, the vibrational response not determined solely by elemental composition, but also influenced by the structural hierarchy of the system.

Phonon hardening, whereas disordered hierarchical assemblies introduce additional phonon scattering and vibrational broadening. Taken together, these findings suggest that nanoscale architectural design can be used to tune the vibrational behavior and thermodynamic of oxide nanotube systems, highlighting interfacial design as a relevant pproach to modulate phonon-mediated energy transport in TiO_2-based nanostructures relevant to photocatalysis, sensing, and energy conversion technologies.

4 Conclusions

The combined structural, spectroscopic, and thermodynamic analyses indicate that anodization parameters and Fe/Cu functionalization influence the morphological hierarchy and interfacial architecture of TiO_2 nanotube arrays while preserving anatase as the dominant phase after annealing at 450 °C. SEM–EDS indicates homogeneous Fe/Cu oxide domains anchored to the nanotubular framework, and optical measurements suggest additional electronic states associated with the surface oxides without altering the intrinsic TiO_2 lattice. Raman spectra together with calorimetric measurements indicate that lattice dynamics are influenced by morphology-driven interfacial coupling. Pristine nanotubes exhibit a thermodynamic state dominated by vibrational entropy, whereas the Fe/Cu-modified architecture shows increased Debye and Einstein temperatures (336.9→393.1 K and 589.6→717.9 K), indicating phonon hardening and enhanced lattice rigidity. These suggest that nanoscale architectural control influences the vibrational behavior and thermodynamic response of TiO_2 nanotube systems, with interfacial morphology acting as an important parameter in phonon-mediated energy transport in oxide nanostructures.

Acknowledgements Special thanks to Professor Paulo de Tarso Cavalcante and Paulo S. Pizani in Brazil for Raman measurements and Professor Jorge Bautista in Colombia for help in the anodizing process. Internationalization Project between Embrapa Instrumentation (Brazil) and Universidad Nacional de Colombia Bogotá (UNAL). FAPESP (2021/14992-1) Brazil.

Author Contributions J.O.D. Malafatti and E.C. Paris contributed to experimental work and manuscript writing. D.E. Bernal Lozano performed measurements and data analysis. J. Barba-Ortega contributed to conceptualization and scientific discussion. M.R. Joya conducted experiments, developed the methodology, supervised the research, interpreted the results, and prepared the original manuscript. All authors contributed to the review and editing of the manuscript and approved the final version.

Funding Open Access funding provided by Colombia Consortium

Data Availability The datasets generated and analyzed during the current study are available from the corresponding author upon reasonable request.

Declarations

Conflicts of Interest The authors declare that they have no conflict of interest.

References

1. M. Liao, H. Ma, D. Yu, H. Han, X. Xu, X. Zhu, Formation mechanism of anodic titanium oxide in mixed electrolytes. Mater. Res. Bull. **95**, 539–545 (2017). https://doi.org/10.1016/j.materresbull.2017.08.041

2. O. Zakir, R. Idouhli, M. Elyaagoubi, M. Khadiri, A. Aityoub, Y. Koumya, S. Rafqa, A. Abouelfida, A. Outzourhit, Fabrication of TiO_2 nanotube by electrochemical anodization: Toward photocatalytic application. J. Nanomater. **2020**, 4745726 (2020). https://doi.org/10.1155/2020/4745726
3. V. Sivaprakash, R. Narayanan, Synthesis of TiO_2 nanotubes via electrochemical anodization with different water content. Mater. Today Proc. **37**, 142–146 (2021). https://doi.org/10.1016/j.matpr.2020.04.657
4. D.M. Duc, L.V. Toan, V.C. Manh et al., Effect of anodization time on the structure, corrosion resistance, and biocompatibility of TiO_2 nanotubes formed at 5 °C. J. Mater. Eng. Perform. (2026). https://doi.org/10.1007/s11665-026-13526-6
5. A. Sandoval-Amador, J. Niño, J.F. Lopez-Rincon et al., Influence of anodization conditions in hydrofluoric acid electrolyte on the optimization of TiO_2 nanotube surfaces. Appl. Phys. A **131**, 609 (2025). https://doi.org/10.1007/s00339-025-08743-0
6. O. Zakir, A. Ait-Karra, R. Idouhli, M. Khadiri, B. Dikici, A. Aityoub, A. Abouelfida, A. Outzourhit, Effect of anodization time on the morphological, structural, electrochemical, and photocatalytic properties of anodic TiO_2 NTs. J. Solid State Chem. **322**, 123939 (2023). https://doi.org/10.1016/j.jssc.2023.123939
7. S. Zhang, X. Gong, Q. Shi, G. Ping, H. Xu, A. Waleed, G. Li, CuO nanoparticle-decorated TiO_2 nanotube heterojunctions for direct synthesis of methyl formate via photo-oxidation of methanol. ACS Omega **5**(26), 15942–15948 (2020). https://doi.org/10.1021/acsomega.0c01169
8. O. Zakir, A. Ait Karra, R. Idouhli et al., Fabrication and characterization of Ag- and Cu-doped TiO_2 nanotubes by in situ anodization method as an efficient photocatalyst. J. Solid State Electrochem. **26**, 2247–2260 (2022). https://doi.org/10.1007/s10008-022-05237-4
9. M.T. Acar, H. Kovacı, A. Çelik, Improving the wettability and corrosion behavior of Cp-Ti by applying anodization surface treatment with the addition of boric acid, graphene oxide and hydroxyapatite. Mater. Today Commun. **31**, 103683 (2022). https://doi.org/10.1016/j.mtcomm.2022.103683
10. K. Indira, U.K. Mudali, T. Nishimura et al., A review on TiO_2 nanotubes: influence of anodization parameters, formation mechanism, properties, corrosion behavior, and biomedical applications. J. Bio-Tribo-Corros. **1**, 28 (2015). https://doi.org/10.1007/s40735-015-0024-x
11. J. Grotberg, A. Hamlekhan, A. Butt, S. Patel, D. Royhman, T. Shokuhfar, C. Sukotjo, C. Takoudis, M.T. Mathew, Thermally oxidized titania nanotubes enhance the corrosion resistance of Ti6Al4V. Mater. Sci. Eng., C **59**, 677–689 (2016). https://doi.org/10.1016/j.msec.2015.10.056
12. K.F.L. Dos Anjos, C.D.C. da Silva, M.A.A. de Souza, A.B. de Mattos, L.C.B.B. Coelho, G. Machado, J.V. de Melo, R.C.B.Q. de Figueiredo, The deposition of a lectin from Oreochromis niloticus on the surface of titanium dioxide nanotubes improved the cell adhesion, proliferation, and osteogenic activity of osteoblast-like cells. Biomolecules **11**(12), 1748 (2021). https://doi.org/10.3390/biom11121748
13. A. Laongdao, P. Mali, Shear bond strength of lithium disilicate bonded with various surface-treated titanium. Int. J. Dent. **2022**, 4406703 (2022). https://doi.org/10.1155/2022/4406703
14. M. Misriyani, A. Wahab, P. Taba, J. Gunlazuardi, Effect of anodizing time and annealing temperature on photoelectrochemical properties of anodized TiO_2 nanotube for corrosion prevention application. Indones. J. Chem. **17**(2), 219–227 (2017). https://doi.org/10.22146/ijc.24183
15. I.C. Tatar, N. Cicek, Anodization of Ti6Al4V in water-ethylene glycol solution containing NH_4F and its corrosion behavior in Ringer's solution. Int. J. Electrochem. Sci. **17**, 220624 (2022). https://doi.org/10.20964/2022.06.33
16. K. Mukta, M. Anca, S. Patrik, I. Ales, Influence of anodization parameters on morphology of TiO_2 nanostructured surfaces. Adv. Mater. Lett. **7**, 23–28 (2016). https://doi.org/10.5185/AMLETT.2016.6156
17. N.S. Leyland, J. Podporska-Carroll, J. Browne, S.J. Hinder, B. Quilty, S.C. Pillai, Highly efficient F, Cu doped TiO_2 antibacterial visible light active photocatalytic coatings to combat hospital-acquired infections. Sci. Rep. **6**, 24770 (2016). https://doi.org/10.1038/srep24770
18. S. Dai, L. Liu, Z. Wang, H. Deng, L. Zhou, J. Cui, Z. Su, L. Xu, L. Yao, P. Yang, UV-modified and dual-catalytic Cu porphyrin-loaded TiO_2 nanotubes with enhanced hemocompatibility and prevention of stent restenosis. Mater. Today Commun. **35**, 106297 (2023). https://doi.org/10.1016/j.mtcomm.2023.106297
19. C. Dames, B. Poudel, W.Z. Wang, J.Y. Huang, Z.F. Ren, Y. Sun, J.I. Oh, C. Opeil, M.J. Naughton, G. Chen, Low-dimensional phonon specific heat of titanium dioxide nanotubes. Appl. Phys. Lett. **87**, 031901 (2005). https://doi.org/10.1063/1.1990269
20. Y. Wang, T. Feng, X. Li, L. Li, Thermochemistry of nano-phased titanium dioxides relevant to energy application: A review. Chem. Thermodyn. Therm. Anal. **5**, 10003 (2022). https://doi.org/10.1016/j.ctta.2021.10003
21. T. Feng, L. Li, Q. Shi, Y. Zhang, G. Li, Heat capacity and thermodynamic functions of TiO_2(H). J. Chem. Thermodyn. **145**, 106040 (2020). https://doi.org/10.1016/j.jct.2019.106040
22. H.M. Mateus, J. Barba-Ortega, M.R. Joya, Comparison of the growth of TiO_2 nanotubes in different solutions. J. Inorg. Organomet. Polym Mater. **28**, 612–623 (2018). https://doi.org/10.1007/s10904-018-0783-1
23. H.M. Mateus, J. Bautista-Ruiz, J. Barba-Ortega, M.R. Joya, Formation of titanium oxide nanotube arrays by controlling H_2O and time through anodic oxidation. Rasayan J. Chem. **12**, 1304–1314 (2019). https://doi.org/10.31788/RJC.2019.1235265
24. M.R. Joya, J. Barba-Ortega, E.C. Paris, Obtención de muestras de óxidos a bajo costo. Rev. UIS Ing. **18**(3), 33–37 (2019). https://doi.org/10.18273/revuin.v18n3-201900
25. J. Bautista-Ruiz, W. Aperador, M.R. Joya, Electrochemical impedance, cyclic voltammetry, and corrosive behavior in TiO_2 nanostructures. Rasayan J. Chem. **13**(4), 2092–2098 (2020). https://doi.org/10.31788/RJC.2020.1345854
26. W.A. Aperador-Chaparro, J. Barba-Ortega, M.R. Rincón-Joya, Optimization of corrosion resistance of anodized TiO_2 coatings through controlled calcination parameters. Rev. Acad. Colomb. Cienc. Exactas Fís. Nat. **48**(188), 483–490 (2024). https://doi.org/10.18257/raccefyn.2652
27. H.-S. Heo, S.-J. Kim, Investigation of electrochemical characteristics and interfacial contact resistance of TiN-coated titanium as bipolar plate in polymer electrolyte membrane fuel cell. Coatings **13**, 123 (2023). https://doi.org/10.3390/coatings13010123
28. H. Sopha, Z. Spotz, M. Sepúlveda, M. Alijani, M. Motola, L. Hromadko, J.M. Macak, Intrinsic properties of anodic TiO_2 nanotube layers: In-situ XRD annealing of TiO_2 nanotube layers. Ceram. Int. **49**(14), 24293–24301 (2023). https://doi.org/10.1016/j.ceramint.2022.11.032
29. M.Y. Roshchina, C.J. Querebillo, E. Dmitrieva, A. Voss, N. Israel, T. Gemming, L. Giebeler, S. Pilz, S. Roeher, V. Hoffmann, M. Hantusch, I.M. Weidinger, A. Gebert, Corrosion behavior of an oxide nanotube-coated β-type Ti-45Nb implant alloy in a simulated inflammatory solution. Corros. Sci. **227**, 111767 (2024). https://doi.org/10.1016/j.corsci.2023.111767
30. S. Ait Ali Yahia, L. Hamadou, A. Kadri, N. Benbrahim, E.M.M. Sutter, Effect of anodizing potential on the formation and EIS characteristics of TiO_2 nanotube arrays. J. Electrochem. Soc. **159**(4), K83–K90 (2012). https://doi.org/10.1149/2.077204jes
31. M. Yoon, Y. Park, H. Sim, H.R. Kwon, Y. Lee, H.W. Jang, S.-Y. Choi, J. Son, 2D vacancy confinement in anatase TiO_2 for

enhanced photocatalytic activities. Adv. Mater. **37**(15), 2413062 (2025). https://doi.org/10.1002/adma.202413062
32. N. Madima, N.M. Chauke, S. Ngqoloda, O.K. Mmelesi, M. Raphulu, Recent advances in the development of defective black TiO_2 nanomaterials for application in energy and environmental sustainability: A review. Results Eng. **26**, 104868 (2025). https://doi.org/10.1016/j.rineng.2025.104868
33. J.A. Benavides-Guerrero, P. Fourmont, L.F. Gerlein, A.C. Angel-Ospina, F. Machuca-Martinez, F. Vaussenat, C.A. Ross, S.G. Cloutier, Black anatase-TiO_2 electrodes for sun-activated photocatalytic degradation of organic water contaminants. Surf. Interfaces. **58**, 105849 (2025). https://doi.org/10.1016/j.surfin.2025.105849
34. M.A. Hossen, A. Abd Aziz, R. Ramadhan Ikreedeegh, A.D. Muhammad, N. Yaacof, K.H. Leong, L. Wu, Optimization of anodizing parameters for the morphological properties of TiO_2 nanotubes based on response surface methodology. Results Mater. **14**, 100061 (2024). https://doi.org/10.1016/j.rinma.2023.100061
35. P. Roy, S. Berger, P. Schmuki, TiO_2 nanotubes: synthesis and applications. Angew. Chem. Int. Ed. **50**, 2904–2939 (2011). https://doi.org/10.1002/anie.201001374
36. S.P. Gajagouni, I. Barsoum, S.O. Cho, A. Alfantazi, Corrosion behavior of anodized nanoporous TiO_2 films in oxidizing environments: A study on electrochemically engineered titanium surfaces. Nanoscale Adv. **7**(23), 7579–7587 (2025)
37. I. Paramasivam, H. Jha, N. Liu, P. Schmuki, A review of photocatalysis using self-organized TiO_2 nanotubes and other ordered oxide nanostructures. Small **8**, 3073–3103 (2012). https://doi.org/10.1002/smll.201200564
38. C.-C. Chiang, J.-S. Li, H.-H. Wan, F. Ren, J.F. Esquivel-Upshaw, Fabrication of TiO_2 nanotube arrays by progressive anodization of Ti thin film on insulated substrates. Materials. **18**(6), 1219 (2025). https://doi.org/10.3390/ma18061219
39. U. Diebold, The surface science of titanium dioxide. Surf. Sci. Rep. **48**(5–8), 53–229 (2003). https://doi.org/10.1016/S0167-5729(02)00100-0
40. Y. Zhang, W. Wu, K. Zhang, C. Liu, A. Yu, M. Peng, J. Zhai, Raman study of 2D anatase TiO_2 nanosheets. Phys. Chem. Chem. Phys. **18**, 32178–32184 (2016). https://doi.org/10.1039/C6CP05496J
41. S. Harini, G. Gupta, S.C. Roy, R. Yalavarthi, TiO_2 multi-leg nanotubes for surface-enhanced Raman scattering. J. Phys. D Appl. Phys. **57**, 325106 (2024). https://doi.org/10.1088/1361-6463/ad42a9
42. X. Pan, M.-Q. Yang, X. Fu, N. Zhang, Y.-J. Xu, Defective TiO_2 with oxygen vacancies: synthesis, properties and photocatalytic applications. Nanoscale **5**, 3601–3614 (2013). https://doi.org/10.1039/C3NR00476G
43. X. Che, L. Li, J. Zheng, G. Li, Q. Shi, Heat capacity and thermodynamic functions of brookite TiO_2. J. Chem. Thermodyn. **93**, 45–51 (2016). https://doi.org/10.1016/j.jct.2015.09.018
44. A. Tari, *The Specific Heat of Matter at Low Temperatures*. (Imperial College Press, London, 2003). https://doi.org/10.1142/p254
45. N.W. Ashcroft, N.D. Mermin, *Solid State Physics* (Holt, Rinehart and Winston, New York, 1976)
46. E.J. Cope, J. Bustamante, Z.M. Johnson, R. Gurunathan, J. George, M.T. Agne, Heat capacity estimation of complex materials for energy technologies. J. Mater. Chem. A. **9**, 102054 (2025)